Nanoscale

PAPER

View Article Online
View Journal | View Issue

Published on 07 July 2020. Downloaded by City University of Hong Kong Library on 8/26/2020 2:37:43 PM.

Check for updates

Cite this: *Nanoscale*, 2020, **12**, 16153

High-mobility In and Ga co-doped ZnO nanowires for high-performance transistors and ultraviolet photodetectors†

Fangzhou Li,[a,b] You Meng,[a] Xiaolin Kang,[a] SenPo Yip,[a,b,c,d] Xiuming Bu,[a,b] Heng Zhang[a,b,c] and Johnny C. Ho *[a,b,c,d]

Due to their unique properties, ZnO nanostructures have received considerable attention for application in electronics and optoelectronics; however, intrinsic ZnO nanomaterials usually suffer from large concentrations of lattice defects, such as oxygen vacancies, which restricts their material performance. Here, for the first time, highly-crystalline In and Ga co-doped ZnO nanowires (NWs) are achieved by ambient-pressure chemical vapor deposition. In contrast to conventional elemental doping, this In and Ga co-doping can not only enhance the carrier concentration, but also suppresses the formation of oxygen vacancies within the host lattice of ZnO NWs. Importantly, this co-doping is also believed to effectively minimize the generation of lattice strain defects due to the optimal ionic sizes of both In and Ga dopants. When configured into field-effect transistors (FETs), these co-doped NWs exhibit an enhanced average electron mobility of 315 $cm^2\ V^{-1}\ s^{-1}$ and an impressive on/off current ratio of 1.87×10^8, which are already higher than those of other previously reported ZnO NW devices. In addition, these NW devices demonstrate efficient ultraviolet photodetection at under 261 nm irradiation with an improved responsivity of $1.41 \times 10^7\ A\ W^{-1}$, an excellent EQE of up to 6.72×10^9 and a fast response time down to 0.32 s. Highly-ordered NW parallel array thin-film transistors and photodetectors are also constructed to demonstrate the promising potential of the NWs for high-performance device applications.

Received 14th May 2020,
Accepted 7th July 2020

DOI: 10.1039/d0nr03740k

rsc.li/nanoscale

Introduction

Over the past decades, because of the appropriately wide direct band gap (3.37 eV at room temperature) and large exciton binding energy (60 meV), ZnO nanomaterials have attracted considerable interest as active ingredients for electronic and optoelectronic devices.[1] Due to these unique properties, they are not only interesting materials but also contribute to building blocks for many important technological applications, such as solar cells, electrodes, and gas sensors.[2–4] However, intrinsic ZnO nanomaterials always have large concentrations of native defects (*e.g.* oxygen vacancies, V_o), which deteriorate their material properties and impose significant restrictions on their practical utilization. In this case, various methods have been extensively explored to suppress the adverse effects of V_o defects on the electrical and optical properties of ZnO nanostructures. Doping with foreign atoms is generally an effective technique to inherently manipulate the properties of host materials.[5–7] Even though there have been many recent advances in the fabrication of ZnO nanomaterials with different dopants, including Al, Ga and In,[8,9] it is still a great challenge to achieve enhanced one-dimensional (1D) ZnO nanowire (NW) materials with uniform doping, excellent crystallinity and superior electrical properties for the excellent performance of subsequently fabricated devices.

Among many dopants, proper doping with In atoms has been demonstrated to improve the properties of ZnO nanostructures.[10,11] To be specific, optimal In-doped ZnO nanostructures exhibit enhanced optical transmission, better chemical stability, superior thermal stability and, more importantly, higher electrical conductivity. Once configured into field-effect transistors (FETs), they can deliver high output current density and carrier mobility, as In dopants have extended 5s orbitals that easily overlap with the orbitals of the host lattice to form efficient electron conducting pathways.[12] ZnO nanomaterials are also broadly investigated for transpar-

[a]*Department of Materials Science and Engineering, City University of Hong Kong, Kowloon 999077, Hong Kong SAR. E-mail: johnnyho@cityu.edu.hk*
[b]*Shenzhen Research Institute, City University of Hong Kong, Shenzhen 518057, P.R. China*
[c]*State Key Laboratory of Terahertz and Millimeter Waves, City University of Hong Kong, Kowloon 999077, Hong Kong SAR*
[d]*Centre for Functional Photonics, City University of Hong Kong, Kowloon 999077, Hong Kong SAR*

†Electronic supplementary information (ESI) available. See DOI: 10.1039/d0nr03740k

Published on 07 July 2020. Downloaded by City University of Hong Kong Library on 8/26/2020 2:37:43 PM.

ent electronics, which have an extremely large potential global market.[13] Unfortunately, there are still several drawbacks associated with In-doped ZnO nanostructures. One issue is that because In serves as a n-type dopant for intrinsically n-type ZnO, the processed nanomaterials inevitably have an excess free electron concentration after doping; therefore, the fabricated devices require a high gate bias to deplete the channel electrons for the off-state of the device.[14] Additionally, In doping tends to induce more V_o defects in the ZnO host lattice, which donate additional free electrons to the device channel and further lead to degradation of the transistor performance.[15] For example, Zhu *et al.* recently fabricated In-doped ZnO nanorod devices with a large on current of around 6.39×10^4 A but also with a high off current compared with their pristine ZnO counterparts; this high off current mainly arises from increased V_o defects, as confirmed by the XPS characterization.[14] Similar results were reported by Park and co-workers, who stated that In-doped ZnO nanostructures tend to possess higher concentrations of V_o defects.[16]

On the other hand, it is interesting that Ga-doped ZnO nanorods are found to have lower V_o concentrations in contrast to pure and In-doped ZnO nanorods.[16] Due to the small ionic radius of Ga, these dopants can easily bind with oxygen constituents to lessen the formation of V_o defects.[17] Moreover, Ga-doped ZnO NW devices can deliver better electron mobility than undoped NW devices by simply increasing the Ga doping concentration in the NW channel; this mobility enhancement is attributed to the saturation of V_o defects.[18] However, further increasing the Ga doping concentration reduces the electron mobility because of enhanced electron scattering by Ga impurities. Inevitably, a high doping concentration significantly increases the amount of lattice strain because of the lattice mismatch between the dopant atoms and the host lattice. This lattice strain would reduce the solid solubility of the dopants in ZnO and also initiate lattice defects for the uncontrolled carrier concentration.[19] Therefore, it is difficult to only increase the doping concentration sufficiently to obtain enhanced properties without generating any ionized impurity scattering centers and strain defects within the lattice.[20] In fact, for the thin-film device community, multiple elements are usually employed as co-dopants for ZnO channels in order to manipulate their device characteristics.[21–23] At the same time, these doping schemes can improve device stability under bias stress and light illumination.[24–26] To date, no similar studies have been performed for ZnO NWs; hence, it is crucial to explore the electrical and optical properties of ZnO NWs by utilizing these doping arrangements.

In this work, for the first time, crystalline In and Ga co-doped ZnO NWs with uniform diameters and morphologies are successfully achieved by ambient-pressure chemical vapor deposition (CVD). In and Ga dopants are chosen because In doping can increase the free carrier concentration of ZnO NWs, while the incorporation of Ga helps to suppress the generation of V_o defects due to the relatively high binding energy of Ga–O bonds compared with those of In–O and Zn–O bonds. It is also worth mentioning that this In and Ga co-doping is anticipated to minimize doping-induced lattice strain because In^{2+} has a larger ionic radius (81 pm) and Ga^{3+} has a smaller ionic radius (62 pm) compared with Zn^{2+} (74 pm). As a result, the electrical properties of ZnO NWs can be improved by incorporating both In and Ga dopants without sacrificing their electron mobility due to the reduced V_o defects and other strain defects within the lattice. Explicitly, when fabricated into FETs, a single In and Ga co-doped ZnO NW device can deliver an impressively high on/off current ratio of 1.9×10^8 and a superior average electron mobility of 315 $cm^2\ V^{-1}\ s^{-1}$, which are significantly better than those of other state-of-the-art ZnO NW transistors. Importantly, the optimized NW device can also serve as a high-performance ultraviolet (UV) photodetector, exhibiting a high responsivity of 1.41×10^7 A W^{-1} and a large EQE of up to 6.72×10^9 at under 261 nm irradiation. The detector response times are determined to be 0.3 and 0.8 s for the rise and decay times, respectively. Highly-ordered NW parallel array transistors and photodetectors are also constructed and showed excellent performance. All these results evidently demonstrate the promising potential of In and Ga co-doped ZnO NWs for next-generation electronic and optoelectronic applications.

Experimental section

Nanowire synthesis

The In and Ga co-doped ZnO NWs and pristine ZnO NWs were synthesized by ambient-pressure CVD. p^+-Si/SiO_2 (50 nm-thick thermal oxide) pieces were employed as the substrates, whereas Au catalysts (0.1 nm in nominal thickness) were thermally evaporated onto the substrate for subsequent NW growth. For the case of In and Ga co-doped NWs, zinc powder (0.0025 g; 20–30 mesh; >99.8% purity; Sigma-Aldrich), In granules (0.3 g; 1–2 mm in size; 99.999% purity; China Rare Metal) and Ga granules (0.15 g; 1–2 mm in size; 99.999% purity; China Rare Metal) were mixed with graphite powder (0.3 g; <20 μm in size; synthetic; Sigma-Aldrich), which was utilized as the precursor source. A small quartz tube (1 cm in diameter) with a length of 10 cm was used to hold the source at the sealed end with the substrate placed at the open end. The complete setup was then placed in the center of a large quartz tube (1 inch in diameter) and heated to 1010 °C in 20 min. This temperature was maintained for 10 min with the flow rates of the gas mixture (10% vol oxygen and 90% vol argon) and argon (99.9995% purity) maintained at 20 and 80 sccm, respectively. Once the reaction was complete, the system was naturally cooled. The entire process was then repeated one more time with the same precursor source but with fresh substrates, with the growth duration increased to 20 min. In this way, the In and Ga co-doped ZnO NWs were obtained for the second growth runs, as shown in Fig. S1.† For the case of the pristine ZnO NWs, only the same amount of zinc powder was utilized as the source, while the flow rates of the gas mixture and argon were changed to 5 sscm and 100 sscm, accordingly. The complete system was then heated to 1000 °C in 20 min

 This journal is © The Royal Society of Chemistry 2020

Published on 07 July 2020. Downloaded by City University of Hong Kong Library on 8/26/2020 2:37:43 PM.

and held at this temperature for 50 min. After that, the growth was terminated and the system was naturally cooled to room temperature.

Material characterization

X-ray diffraction (XRD, D2 Phaser, Brucker), high-resolution transmission electron microscopy (HRTEM, JEOL-2001F) and selected area electron diffraction (SAED) were employed to characterize the crystal structures of the obtained NWs. The surface morphologies of the NWs were examined by scanning electron microscopy (SEM, Quanta 450 FEG, FEI) and TEM (CM 20, Philips). The chemical compositions of the grown NWs were evaluated by energy dispersive X-ray spectroscopy (EDS) and corresponding elemental mappings. The photoluminescence (PL) spectra of the NWs were collected by an iHR320 PL spectroscope with an excitation wavelength of 325 nm.

Device fabrication and characterization

First, the grown NWs were drop-casted onto p^+-Si/SiO_2 substrates. Next, the source and drain electrode regions were defined by a standard photolithography technique. Then, a layer of 80 nm-thick Ni film was deposited by electron-beam evaporation followed by a lift-off process to obtain the electrodes. In order to protect the device from the ambient environment, a 30 nm-thick Al_2O_3 passivation layer was deposited by e-beam evaporation, and the complete device was baked on a hot plate at 100 °C for 5 h. Finally, the device characterization was performed using a standard probe station with an Agilent 4155C semiconductor analyzer (Agilent Technologies, Santa Clara, CA, USA). A 261 nm laser was used as the light source for the photodetector measurements, and its power density was measured by a power meter (PM400, Thorlabs).

Results and discussion

As depicted in the SEM images (Fig. 1a and c), the obtained In and Ga co-doped ZnO and pristine ZnO NWs are straight, dense and smooth, with lengths of more than 10 μm. Sphere-like catalytic seeds are also observed (Fig. 1b and d), suggesting that the NWs are grown *via* a vapor–liquid–solid (VLS) growth mechanism. Furthermore, the phase purities and crystal structures of the NWs are studied by XRD, where they are indexed to the hexagonal structure of ZnO (PDF no. 36-1451) (Fig. S2†). Apart from the diffraction peaks of ZnO and Si (200) associated with the substrate,[27] no other impurity phases are observed, which indicates the high phase purity of the grown NWs. Moreover, TOPAS software is used to perform Rietveld refinement of the XRD results, as shown in Fig. S3a and b.† As presented in Fig. S3c,† the lattice constants slightly increase after In and Ga co-doping, which suggests the substitution of In and Ga at the Zn sites. The crystallite sizes (D) and strains are compiled in Fig. S3d.† D is calculated using the Debye–Scherrer equation as $D = (18\,000\lambda)/(\pi L_X)$, while the strain is determined using the equation $S = (\pi L_y)/18\,000$, where

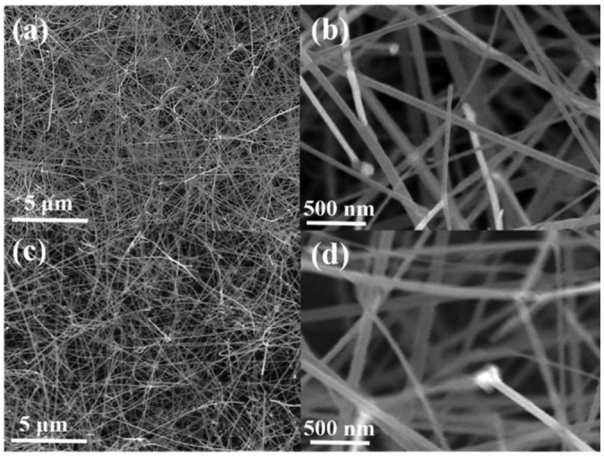

Fig. 1 (a) and (b) SEM images of the obtained In and Ga co-doped ZnO NWs with different magnifications. (c) and (d) SEM images of the obtained pristine ZnO NWs with different magnifications.

L_x and L_y are parameters extracted from the Rietveld refinement. It is clear that the crystallite size of the materials increases from 62.4 nm (ZnO) to 88.4 nm (In and Ga co-doped ZnO). This increased crystallite size is possibly related to the decreased strain (*i.e.* from 0.07 to 0.01) in the lattice associated with the In and Ga co-doping. The room-temperature Raman spectra of the NW samples are also measured in the range of 200–1200 cm^{-1}, revealing several phonon modes associated with the wurtzite ZnO structure[28] (Fig. S4a†). In this case, the lattice strain can also be calculated from the shift of the A_1(TO) peak using the following equation:

$$\varepsilon = \Delta\omega^* \frac{A_1(\mathrm{TO})^* C_{33}}{2(b^* C_{13} - a^* C_{33})} \quad (1)$$

where ε is the in-plane strain, $\Delta\omega = \omega - \omega_o$, ω is the frequency of the A_1 (TO) mode, and ω_o = 379 cm^{-1}. The parameters of a and b are the phonon deformation potential constants for the A_1 (TO) mode, in which a = −774 cm^{-1} and b = −375 cm^{-1} with elastic constants of C_{33} = 216 GPa and C_{13} = 104 GPa.[29] As depicted in Fig. S4b,† it is again confirmed that the strain decreases with the In and Ga co-doping, which is perfectly consistent with the XRD analysis above. In this way, the reduced lattice strain suppresses the formation of lattice defects, which can improve the crystal quality of NWs for subsequent device studies.

At the same time, EDS is employed to assess the chemical composition of the NWs. Obviously, In, Ga, Zn and O signals can be clearly witnessed in the typical EDS spectra of the In and Ga co-doped NWs (Fig. S5a†), suggesting the effective incorporation of both In and Ga into the ZnO NWs. On the other hand, only Zn and O signals are observed for the pristine ZnO control sample (Fig. S5b†). Combined with the relatively small concentration variations of In and Ga in more than 20 of the NW samples (*i.e.* In concentration = 1.1 ± 0.3 at% and Ga concentration = 3.2 ± 0.5 at% in Fig. S6†), these results further illustrate the uniformity of In and Ga co-doping in the NWs

Published on 07 July 2020. Downloaded by City University of Hong Kong Library on 8/26/2020 2:37:43 PM.

using this growth scheme. Based on the statistics of more than 40 individual NWs, the diameter (d) distributions are found to be 43.2 ± 8.8 nm for the In and Ga co-doped ZnO NWs and 73.4 ± 18.4 nm for the pristine ZnO NWs (Fig. S7†). When the In and Ga dopants are introduced into the ZnO NWs, the diameter is observed to be significantly reduced compared with that of the pristine NWs, even when using the same catalyst thickness for the growth. This diameter reduction perfectly agrees with previous studies in which the existence of Ga assists the transport of oxygen vapor and substantially decreases the radial NW growth to achieve thin and uniform NWs.[30] All these findings can facilitate more thorough understanding of the In and Ga co-doped ZnO NW synthesis.

In addition, detailed TEM studies together with SAED characterization are carried out to evaluate the crystallinity and morphology of the obtained NWs. As presented in the TEM images (Fig. 2a and b), the In and Ga co-doped ZnO NWs have a typical diameter of 45 nm, which is significantly thinner than that of the pristine NWs (95 nm); this is consistent with the discussion above. In any case, both NWs have smooth surfaces and constant diameters along the entire length without any tapering. As illustrated in the insets of Fig. 2a and b, SAED is employed to assess the dominant growth orientation and to confirm the crystallinity of the NWs. From the SAED patterns, the undoped ZnO NW has a typical growth direction of ⟨001⟩; meanwhile, for the In and Ga co-doped ZnO NWs, the growth direction changes to ⟨100⟩. To obtain more information about the growth orientation of the In and Ga co-doped ZnO NWs, growth orientation statistics are determined by evaluating the growth directions of 15 different NWs, as shown in Fig. S8.† It is observed that the growth direction of ⟨100⟩ accounts for 54% of the examined NWs, coupled with other growth directions of ⟨110⟩, ⟨001⟩ and ⟨101⟩. Because the growth direction is mostly dictated by the lowest free energy surface of the NW, the growth of pristine ZnO tends to follow the direction of ⟨001⟩, which has the lowest free energy surface. When In, Ga and Zn are used as the precursor sources, the vapors of In and Ga generated in the source may lead to energy variation between the catalyst and the nanowires, switching the NW growth orientation as reported before.[18] In this case, it is unsurprising that the In and Ga co-doping would change the growth direction of the ZnO NWs here, whereas all the results are in good agreement with the SEM and XRD results discussed above. The clear lattice fringes further demonstrate the single crystallinity of the NWs (Fig. 2c and d). Specifically, the lattice spacings of the {002} and {110} planes are found to be very similar between these two types of ZnO NWs; this suggests that the In and Ga co-doping does not induce any significant lattice strain on the host lattice, in distinct contrast to the large amounts of lattice strain induced in conventional elemental doping. Additionally, STEM coupled with elemental mappings is performed on the individual NWs. For the case of the In and Ga co-doped ZnO NW, it is obvious that the In, Ga, Zn and O constituents are all homogenously distributed along the NW (Fig. 2e). These TEM results reveal the uniform co-doping of In and Ga within the ZnO lattice without generating any significant morphological or lattice defects.

To shed light on the electrical properties of the prepared NWs, global back-gated FET devices based on the single NWs are fabricated, and their transfer and output characteristics are measured in ambient conditions. Fig. 3a shows the SEM image of a typical device and its schematic (inset). It is clear

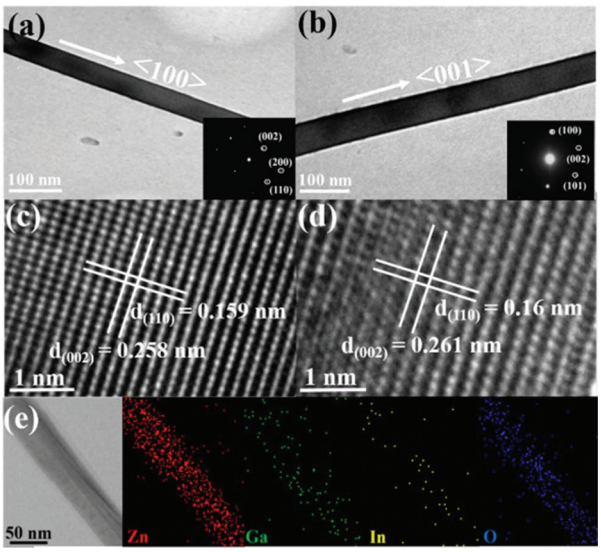

Fig. 2 (a) and (b) TEM images and corresponding SAED patterns (insets) of an In and Ga co-doped ZnO NW and a pristine ZnO NW, respectively. (c) and (d) HRTEM images of the In and Ga co-doped ZnO NW and the pristine ZnO NW, accordingly. (e) STEM image and corresponding elemental mappings of the Zn, Ga, In, and O constituents of the In and Ga co-doped ZnO NW.

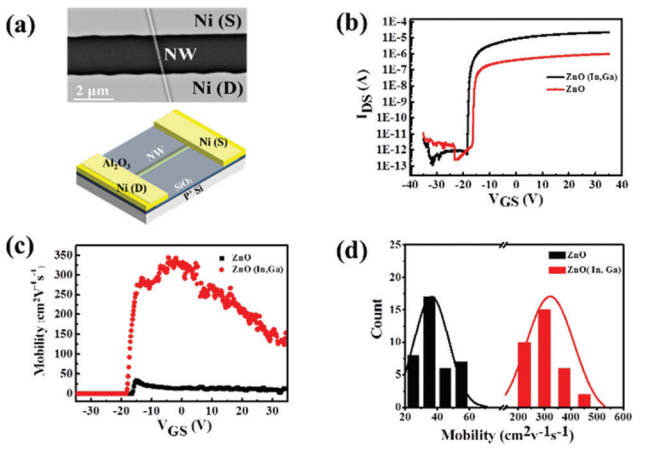

Fig. 3 (a) SEM image (top) and device schematic (bottom) of a typical In and Ga co-doped ZnO NW FET. (b) Transport characteristics of the FETs based on the In and Ga co-doped ZnO NWs and the pristine ZnO NWs. All devices are surface-passivated with a 30 nm-thick Al_2O_3 layer and V_{DS} = 1 V. (c) Field-effect electron mobility assessment for the same set of FETs presented in panel b. (d) Statistical results of the peak field-effect electron mobility of 40 different NW FETs for each sample group with their respective Gaussian fittings. The scan rate is 500 mV s^{-1} for panels b and c.

This journal is © The Royal Society of Chemistry 2020

Published on 07 July 2020. Downloaded by City University of Hong Kong Library on 8/26/2020 2:37:43 PM.

Table 1 Comparison of the performance parameters among ZnO NW devices investigated in this work and other state-of-the-art ZnO NW devices reported in the literature

FET device	V_{DS} (V)	On/off current ratio	On current (*A*)	V_{th} (V)	Mobility ($cm^2\ V^{-1}\ s^{-1}$)	Ref.
ZnO NW	0.1	2.6×10^6	—	−6.6	88	34
ZnO NW	1	10^6	—	21.4	60	35
ZnO NW	2	$\sim 10^4$	$\sim 1.6 \times 10^{-6}$	—	>50	36
ZnO NW	5	5.8×10^6	—	7.4	13	37
ZnO NW	1	10^3	1.5×10^{-6}	–	30	38
ZnO NW	0.1	10^4–10^5	2.7×10^{-7}	−2.0	80	39
ZnO NW	10	10^7	—	–	40	40
In-doped ZnO NR	5	10^3	6.4×10^{-4}	−3.3	26	14
ZnO NW	1	4.0×10^6	1.0×10^{-6}	−19.6	36 ± 11	This work
In and Ga Co-doped ZnO NW	1	1.9×10^8	2.2×10^{-5}	−20.5	315 ± 113	This work

that both types of NW devices (*i.e.* In and Ga co-doped ZnO and pristine ZnO) show significant hysteresis in their transfer curves, which is attributed to the adsorption of ambient gas molecules on the NW surface (Fig. S9†). Hence, a layer of 30 nm-thick Al_2O_3 is deposited onto the NW devices for passivation, followed by the evaluation of their transfer and output characteristics. It is observed that the surface passivation can substantially reduce the device hysteresis without degrading the devices' on current, off current and on/off current ratio. Based on the transfer characteristics, both NW devices exhibit n-type conducting behavior. Under a source–drain bias (V_{DS}) of 1 V and a source–gate bias (V_{GS}) of 35 V, the In and Ga co-doped ZnO NW FET delivers an on current of 21.7 μA, an off current of 0.11 pA and an on/off current ratio as high as 1.87×10^8, whereas the pristine ZnO NW FET affords an on current of 0.95 μA, an off current of 0.24 pA and an on/off ratio current of 3.97×10^6 (Fig. 3b). Furthermore, the linear output characteristics confirm the ohmic-like contact between the electrodes and NWs (Fig. S10b and d†). The field-effect electron mobility (μ_{FE}) can then be calculated from the transfer curves utilizing the square law model with the analytical expression $\mu_{FE} = g_m (L^2/C_{ox}) (1/V_{DS})$, where g_m is the transconductance determined by dI_{DS}/dV_{GS}, L is the channel length and C_{ox} is the gate capacitance, which can be accurately obtained from the finite element analysis software COMSOL.[31–33] Explicitly, the peak mobility of a typical In and Ga co-doped ZnO NW device ($d \sim 40$ nm) is found to be 315 $cm^2\ V^{-1}\ s^{-1}$, which is much higher than that (36 $cm^2\ V^{-1}\ s^{-1}$) of the pristine ZnO NW FET ($d \sim 70$ nm) (Fig. 3c). More than 40 NW devices are measured for each sample group to assess their average mobility values (Fig. 3d). It is evident that the average mobility of the In and Ga co-doped ZnO NW FETs is 315 ± 113 $cm^2\ V^{-1}\ s^{-1}$, which is much higher than that of the ZnO NW devices (36 ± 11 $cm^2\ V^{-1}\ s^{-1}$). Although the In and Ga co-doped ZnO NWs have smaller average diameters (*i.e.* smaller effective device channel widths) than the pristine NWs, the co-doped NWs still deliver much higher electron mobility; this clearly indicates that the mobility is enhanced by this co-doping scheme. Also, a slight mobility variation is observed for each sample group; this variation can be attributed to the surface roughness, crystallinity and many other factors of the NWs. In any case, the performance parameters, in particular the electron mobility, of the In and Ga co-doped ZnO NW devices are already better than those of state-of-the-art ZnO NW FETs reported in the literature (Table 1).

In addition to demonstrating excellent NW device performance, it is important to understand the enhancement of the electron mobility of the In and Ga co-doped ZnO NW devices. Hence, XPS is carried out to survey the elemental composition and chemical states of the fabricated ZnO NWs. As shown in Fig. 4a, both In and Ga co-doped ZnO and pristine ZnO NWs consist of Zn, O and C, in which the C signal is always associated with atmospheric contamination caused by air exposure. There are no other impurity peaks, except for the dopants of In and Ga. Their corresponding high-resolution spectra of Zn

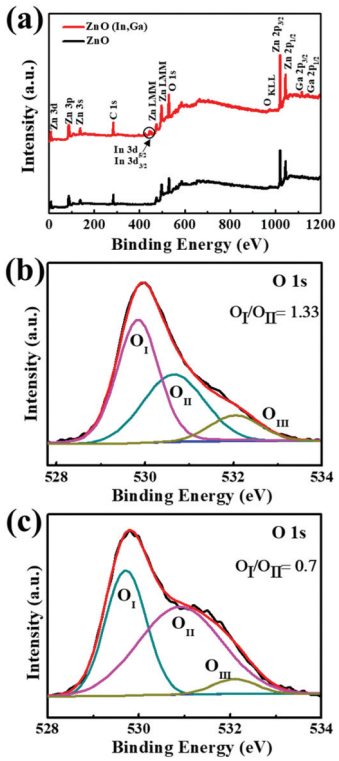

Fig. 4 (a) XPS survey spectra of both In and Ga co-doped ZnO and pristine ZnO NWs. Deconvoluted O 1s spectra of the (b) co-doped ZnO and (c) pristine ZnO NWs, respectively.

Published on 07 July 2020. Downloaded by City University of Hong Kong Library on 8/26/2020 2:37:43 PM.

2p, In 3d and Ga 2p are also presented in Fig. S11a–c,† respectively. It is noted that the presence of metallic In and Ga XPS signals, together with the absence of In_2O_3 and Ga_2O_3 peaks in the XRD pattern (Fig. S2†), clearly confirm the successful incorporation of In and Ga into the ZnO host lattice. More importantly, O 1s spectra are obtained for both samples and are typically deconvoluted into three types of oxygen levels, as shown in Fig. 4b.[16] In general, the lower bonding energy (O_I), located at ~529.7 eV, is attributed to O^{2-} within the ZnO lattice. The medium bonding energy (~531 eV), labeled as O_{II}, is related to the oxygen-deficient regions within the lattice, while the O_{III} components with a higher bonding energy (~532.1 eV) correspond to specific chemisorbed oxygen species, such as H_2O or $-CO_3$. Therefore, the area ratio of O_I/O_{II} is widely employed to demonstrate the relative concentration of oxygen vacancies. These O_I/O_{II} values are determined to be 1.33 for the In and Ga co-doped ZnO NWs and 0.7 for the pristine ZnO NWs, indicating that the co-doped ZnO NWs contain fewer oxygen vacancies; this is attributed to the stronger bonding energy of Ga–O compared to that of Zn–O.[41] In this way, the Ga doping is believed to improve the effectiveness of oxygen bonding with metal constituents to reduce the V_o concentration of the NWs, leading to a minimized free carrier concentration for the lower off current as well as fewer scattering centers for the enhanced electron mobility of the subsequently fabricated NW devices. The In doping can then yield enhanced on current and carrier mobility due to the extended overlapping of its 5s orbitals with those of the other constituents. Again, in contrast with conventional elemental doping, this co-doping alleviates doping-induced lattice strain to suppress the formation of lattice defects for enhanced NW device performance. In addition, room temperature PL spectra of the NWs are obtained, illustrating two emission bands in each spectrum (Fig. S12†). The peak located at ~380 nm is related to the near band edge emission due to the recombination of free excitons of the ZnO NWs; meanwhile, a small red shift of ~3 nm is observed for the In and Ga co-doped sample because of the doping-induced band gap narrowing, changing from 3.21 eV for ZnO to 3.18 eV for In and Ga co-doped ZnO; this is commonly observed in previous literature reports.[42] The other peak at ~550 nm is associated with the O-related native defect states, such as V_o, where the peak intensity is greatly decreased for the co-doped sample. Notably, the PL spectra of these samples are deconvoluted into various emission peaks in different wavelength regions, as displayed in Fig. S13a and b.† These emission peaks correspond to different defects, such as Zn_i, V_o and V_{Zn}, as reported before.[28,43] The relative defect states can be established by calculating the peak intensity ratio (I_{NBE}/I_{DLE}), where NBE and DLE stand for the near band emission and deep level emission, respectively. As shown in Fig. S13c,† the peak intensity ratio of I_{NBE}/I_{DLE} increases after In and Ga co-doping (from 0.56 to 2.12), suggesting decreased defect states of the co-doped NWs. At the same time, multiple Gaussian peaks can be fitted with suitable peak positions, as reported before.[28,43] It can be seen that the emission in the green region, corresponding to V_o defects, and its area percentage ($P_{green} = A_{green}/A_{total}$, $A_{total} = \Sigma A_{all\ regions}$) decrease from 0.86 for the ZnO NWs to 0.52 for the In and Ga co-doped ZnO NWs, suggesting a reduced amount of V_o after co-doping. All these results reveal that suppressed formation of V_o defects is simply achieved through this co-doping scheme.

To explore the practical applications of In and Ga co-doped ZnO NWs, large-scale NW parallel array FETs are fabricated *via* the well-established NW contact printing method, as shown in Fig. 5a.[44,45] After that, the electrical transport properties of the obtained NW parallel array devices are carefully evaluated. It is observed that the typical device delivers a saturation current of 0.39 mA with a current density of 3.9 μA μm^{-1} and a good on/off current ratio of 6.11×10^5 under V_{DS} = 1 V and V_{GS} = 35 V (Fig. 5b). The linear relationship of the output characteristics confirms the ohmic-like contact between the electrodes and NW parallel arrays (Fig. 5c). The corresponding field-effect electron mobility can then be assessed based on the square law model similar to the one performed for the case of the single NW devices in Fig. 3. In this case, the device capacitance is estimated by multiplying the capacitance of a single NW and the total number of NWs in the channel.[46] The peak mobility is calculated to be 115 $cm^2\ V^{-1}\ s^{-1}$, which is on the same level or even better than that of other advanced metal–oxide based thin-film transistors.[47–49] However, the average output current for each NW is somewhat degraded for the NW parallel array devices compared with that of single NW devices, where this degradation can be attributed to inefficient gate coupling due to NW misalignment and broken wires in the channel. Both cases would lead to significant parasitic capacitance, which subsequently deteriorates the output current and switching characteristics of the device. In the future, the NW parallel array device performance can be improved by increasing the NW density, adopting the device structure of high-k dielectrics with top-gated configuration and implementing channel-length scaling. Inevitably, because a diameter distribution of the NWs exists as discussed before,

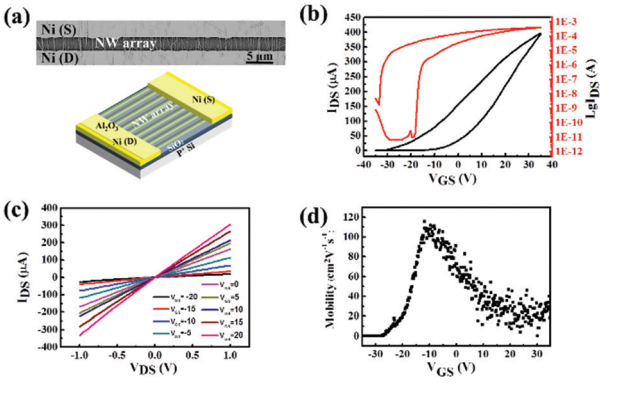

Fig. 5 (a) SEM image (top) and device schematic (bottom) of a typical In and Ga co-doped ZnO NW parallel array FET. (b) Transfer characteristics and (c) output characteristics of the device shown in panel a with a 30 nm-thick Al_2O_3 surface passivation layer (channel length = 2.4 μm; channel width = 100 μm; V_{DS} = 1 V in panel c). (d) Mobility assessment of the NW array device under V_{DS} = 1 V. The scan rate is 500 mV s^{-1} for panels b to d.

This journal is © The Royal Society of Chemistry 2020

Published on 07 July 2020. Downloaded by City University of Hong Kong Library on 8/26/2020 2:37:43 PM.

the diameter of the NWs within the device channel also varies. This dimension difference affects the NW parallel array device characteristics. Therefore, the uniformity of the NW diameter must also be improved to achieve well-controlled device performance. All these results evidently demonstrate the promising potential of high-mobility In and Ga co-doped ZnO NWs for future high-performance thin-film electronics.

In addition to thin-film transistors, these high-mobility In and Ga co-doped ZnO NWs can function as active materials for efficient UV photodetectors. In this work, NW photodetectors employing the back-gated FET structure are fabricated and characterized at under 261 nm irradiation, as depicted in the inset of Fig. 6a. The corresponding current *versus* voltage (*I*–*V*) curves are measured with and without light illumination. The linear *I*–*V* characteristics confirm the ohmic-like contact between the electrodes and NWs. As displayed in Fig. 6a, when the light intensity increases from 0.11 to 0.65 mW cm^{-2}, the output current increases accordingly. In order to study the photosensing properties, the photocurrent (*i.e.* the current difference with and without light illumination) *versus* the light intensity is compiled, as presented in Fig. 6b. The collected data can be well fitted by the power law:

$$I_p = AP^{\theta} \quad (2)$$

where I_p is the photocurrent, A and θ are the fitting parameters and P is the light intensity. The value of θ extracted from the fitting process is determined to be 0.52, indicating a sublinear relationship between the photocurrent and the light intensity; this is attributed to complex processes such as electron–hole pair generation, trapping, and recombination in the device channel.[50] Two additional factors, namely responsivity (R) and external quantum efficiency (EQE), are usually employed to evaluate the performance of photodetectors. They are defined as:

$$R = I_P/(PS) \quad (3)$$

$$\mathrm{EQE} = (hc/e\lambda)\times R \quad (4)$$

where S is the effective area of the photodetector, h is Planck's constant, c is the velocity of light, e is the electronic charge and λ is the exciting wavelength. EQE is measured as a function of light intensity, where the maximum value of EQE was found to be 6.72 × 10^9% (Fig. S14†). As shown in Fig. 6b, R is observed to decrease with increasing light intensity, whereas the maximum value of R is calculated to be 1.41 × 10^7 A W^{-1}. Furthermore, the repeatability of the NW photodetector is characterized by measuring the current *versus* time (*I*–*t*) curves. It is obvious that the device exhibits excellent repeatability, with a respectable on/off current ratio of 1.0 × 10^6 (Fig. 6c). The device response time is then evaluated from the high-resolution *I*–*t* curve. It is noted that for photodetectors based on ZnO, researchers tend to use a double exponential scheme to analyze the response time of the device.[51,52] Typically, for these devices, the response time is composed of two processes: a short process accompanied by a prominent slow process. These types of curves can be well fitted by a double exponential function. However, for a photodetector with fast response, a double exponential scheme cannot be easily used to fit the *I*–*t* curve; therefore, it is difficult to evaluate the response time accurately. As a result, in recent years, for photodetectors based on ZnO with fast response speeds, it is more common to use a different method to calculate the response time.[53–56] Usually, the rise and decay times are defined as the times needed for the current to increase from 10% to 90% of the peak photocurrent and *vice versa*. The rise time and decay time are found to be 0.32 and 0.83 s, respectively (Fig. 6d). The response speeds under different light intensities are also evaluated by a double exponential fitting process, as shown in Fig. S15.† In order to obtain the response time directly and compare it with other work, we employ the transition from 10% to 90% of the peak current and *vice versa* to analyze the response speed here. Once compared with the photodetector fabricated with pristine ZnO NWs (Fig. S16†), the performance parameters of the In and Ga co-doped NW device, such as the responsivity, on/off current ratio and response time, are highly superior, as compiled in Fig. S17.† This enhanced photodetector performance is mostly due to the improved electron mobility of the co-doped ZnO NWs. Notably, these devices already exhibit better photosensing characteristics than other nanostructured materials based on UV photodetectors that have been reported in recent years (Table 2). In addition to the single NW-based devices, photodetectors based on NW parallel arrays are constructed utilizing the same NW contact printing method discussed above for the thin-film transistors. The In and Ga co-doped NW parallel array photodetectors yield effective photoswitching behavior with good repeatability (Fig. S18†). All these findings elucidate

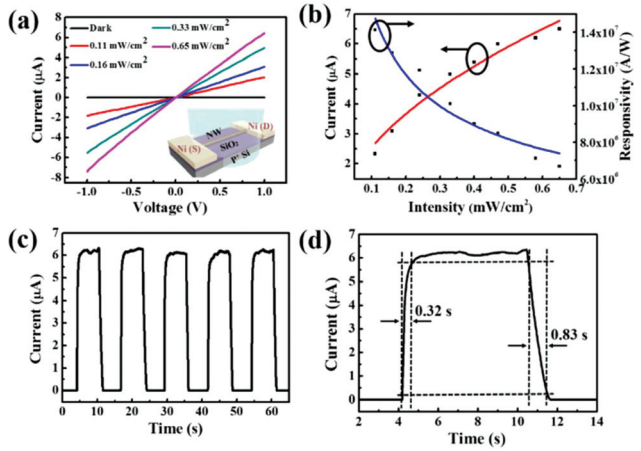

Fig. 6 Current *versus* voltage (*I*–*V*) curves of the In and Ga co-doped ZnO NW photodetector measured in the dark and under different power intensities of 261 nm light illumination. The inset shows the device schematic. (b) The dependence of photocurrent and responsivity as a function of the light intensity. (c) Current *versus* time (*I*–*t*) and (d) high-resolution *I*–*t* curves measured under a light intensity of 0.65 mW cm^{-2}. V_g = −30 V for all panels with the applied bias set as 1 V for panels b to d. The scan rate is 500 mV s^{-1} for panels a and b, whereas the data collection rate is every 30 ms for panels c and d.

Published on 07 July 2020. Downloaded by City University of Hong Kong Library on 8/26/2020 2:37:43 PM.

Table 2 Comparison of the photoresponse characteristics of the In and Ga co-doped ZnO NW photodetector with other nanostructured material-based UV photodetectors reported in recent work

Photodetector	Responsivity (A W^{-1})	EQE (%)	On/off current ratio	Rise time (s)	Decay time (s)	Ref.
g-C_3N_4QDs/ZnO NW	0.4	—	1000	3	5	57
Au NPs/ZnO NW	—	—	5×10^6	25	10	58
Core/Shell ZnO/Cu_xO NW	44.0	149.3	~1	43	43	59
Core/Shell ZnO/ZnSe NW	—	—	233	6	6	60
$CH_3NH_3PbI_3$/ZnO NW	4.0	1300	~8	0.4	0.6	61
ZnO NW	—	—	1000	40	300	62
ZnO/ZnS NW	0.1	—	4	—	—	63
TiO_2/ZnO NW	250	1.6×10^4	140	—	—	64
ZnO/Ag NW	—	—	52	1	0.9	65
In and Ga Co-doped ZnO NW	1.4×10^7	6.7×10^9	1×10^6	0.3	0.8	This work

the promising potency of the In and Ga co-doped NWs for future optoelectronic applications.

Conclusions

In conclusion, crystalline In and Ga co-doped ZnO NWs are successfully fabricated *via* ambient-pressure chemical vapor deposition. The In and Ga dopants work complementarily to enhance the electrical properties of the co-doped NWs. As confirmed by XPS, PL and TEM analysis, the In and Ga co-doping can not only effectively suppress the formation of V_o defects, but can also minimize the doping-induced lattice strain within the ZnO NWs. When fabricated into NW FETs, the In and Ga co-doping leads to enhanced on current and improved electron mobility. To be specific, the FETs deliver an average peak electron mobility of 315 $cm^2\ V^{-1}\ s^{-1}$, which is greatly superior to those of other ZnO NW devices. At the same time, the NWs function as an efficient UV photodetector with an enhanced responsivity of 1.41×10^7 A W^{-1} and an EQE value of around 6.72×10^9% at under 261 nm irradiation. NW parallel array transistors and photodetectors are also constructed to demonstrate the large-scale practical utilization of the NWs. All these results evidently indicate the great potential of In and Ga co-doped ZnO NWs for future high-performance electronic and optoelectronic devices.

Conflicts of interest

There are no conflicts to declare.

Acknowledgements

This work is financially supported by the National Natural Science Foundation of China (Grants 51672229), the General Research Fund (CityU 11275916) and the Theme-based Research (T42-103/16-N) of the Research Grants Council of Hong Kong SAR, China, the Science Technology and Innovation Committee of Shenzhen Municipality (Grant JCYJ20170818095520778) and a grant from the Shenzhen Research Institute, City University of Hong Kong.

Notes and references

1 W.-K. Hong, J. I. Sohn, D.-K. Hwang, S.-S. Kwon, G. Jo, S. Song, S.-M. Kim, H.-J. Ko, S.-J. Park, M. E. Welland and T. Lee, *Nano Lett.*, 2008, **8**, 950–956.
2 C. Soci, A. Zhang, B. Xiang, S. A. Dayeh, D. P. R. Aplin, J. Park, X. Y. Bao, Y. H. Lo and D. Wang, *Nano Lett.*, 2007, **7**, 1003–1009.
3 D.-Y. Son, K.-H. Bae, H.-S. Kim and N.-G. Park, *J. Phys. Chem. C*, 2015, **119**, 10321–10328.
4 R. Kumar, O. Al-Dossary, G. Kumar and A. Umar, *Nano-Micro Lett.*, 2015, **7**, 97–120.
5 W. Peng, J. Yin, K.-T. Ho, O. Ouellette, M. De Bastiani, B. Murali, O. El Tall, C. Shen, X. Miao, J. Pan, E. Alarousu, J.-H. He, B. S. Ooi, O. F. Mohammed, E. Sargent and O. M. Bakr, *Nano Lett.*, 2017, **17**, 4759–4767.
6 G. Gupta, B. Rajasekharan and R. J. E. Hueting, *IEEE Trans. Electron Devices*, 2017, **64**, 3044–3055.
7 K. Ueda, H. Tabata and T. Kawai, *Appl. Phys. Lett.*, 2001, **79**, 988–990.
8 S. Y. Bae, C. W. Na, J. H. Kang and J. Park, *J. Phys. Chem. B*, 2005, **109**, 2526–2531.
9 Y.-S. Kim and W.-P. Tai, *Appl. Surf. Sci.*, 2007, **253**, 4911–4916.
10 S. Young and Y. Liu, *IEEE Trans. Electron Devices*, 2016, **63**, 3160–3164.
11 G. C. Park, S. M. Hwang, S. M. Lee, J. H. Choi, K. M. Song, H. Y. Kim, H.-S. Kim, S.-J. Eum, S.-B. Jung, J. H. Lim and J. Joo, *Sci. Rep.*, 2015, **5**, 10410.
12 K. Nomura, H. Ohta, A. Takagi, T. Kamiya, M. Hirano and H. Hosono, *Nature*, 2004, **432**, 488–492.
13 E. M. C. Fortunato, P. M. C. Barquinha, A. C. M. B. G. Pimentel, A. M. F. Gonçalves, A. J. S. Marques, L. M. N. Pereira and R. F. P. Martins, *Adv. Mater.*, 2005, **17**, 590–594.
14 Z. Zhu, B. Li, J. Wen, Z. Chen, Z. Chen, R. Zhang, S. Ye, G. Fang and J. Qian, *RSC Adv.*, 2017, **7**, 54928–54933.
15 K. W. Liu, M. Sakurai and M. Aono, *J. Appl. Phys.*, 2010, **108**, 043516.
16 G. C. Park, S. M. Hwang, J. H. Choi, Y. H. Kwon, H. K. Cho, S.-W. Kim, J. H. Lim and J. Joo, *Phys. Status Solidi A*, 2013, **210**, 1552–1556.

 This journal is © The Royal Society of Chemistry 2020

Published on 07 July 2020. Downloaded by City University of Hong Kong Library on 8/26/2020 2:37:43 PM.

17 M. H. Kim and H. S. Lee, *Solid-State Electron.*, 2014, **96**, 14–18.
18 G.-D. Yuan, W.-J. Zhang, J.-S. Jie, X. Fan, J.-X. Tang, I. Shafiq, Z.-Z. Ye, C.-S. Lee and S.-T. Lee, *Adv. Mater.*, 2008, **20**, 168–173.
19 J. Zhu, F. Liu, G. B. Stringfellow and S.-H. Wei, *Phys. Rev. Lett.*, 2010, **105**, 195503.
20 G. S. Kar, A. Dhar, L. K. Bera, S. K. Ray, S. John and S. K. Banerjee, *J. Mater. Sci.: Mater. Electron.*, 2002, **13**, 49–55.
21 M. Kumar, T.-H. Kim, S.-S. Kim and B.-T. Lee, *Appl. Phys. Lett.*, 2006, **89**, 112103.
22 E. Senthil Kumar, J. Chatterjee, N. Rama, N. DasGupta and M. S. R. Rao, *ACS Appl. Mater. Interfaces*, 2011, **3**, 1974–1979.
23 L. L. Chen, J. G. Lu, Z. Z. Ye, Y. M. Lin, B. H. Zhao, Y. M. Ye, J. S. Li and L. P. Zhu, *Appl. Phys. Lett.*, 2005, **87**, 252106.
24 Y. Jung, W. Yang, C. Y. Koo, K. Song and J. Moon, *J. Mater. Chem.*, 2012, **22**, 5390–5397.
25 J. Chang, Z. Lin, M. Lin, C. Zhu, J. Zhang and J. Wu, *J. Mater. Chem. C*, 2015, **3**, 1787–1793.
26 H. L. Porter, A. L. Cai, J. F. Muth and J. Narayan, *Appl. Phys. Lett.*, 2005, **86**, 211918.
27 P. Zaumseil, *J. Appl. Crystallogr.*, 2015, **48**, 528–532.
28 P. K. Mishra, S. Ayaz, T. Srivastava, S. Tiwari, R. Meena, B. Kissinquinker, S. Biring and S. Sen, *J. Mater. Sci.: Mater. Electron.*, 2019, **30**, 18686–18695.
29 A. Saniya, P. K. Mishra, R. K. Sharma, S. Kamal and S. Sen, *ACS Appl. Nano Mater.*, 2020, **3**, 4562–4573.
30 Z. Zhou, C. Lan, S. Yip, R. Wei, D. Li, L. Shu and J. C. Ho, *Nano Res.*, 2018, **11**, 5935–5945.
31 Z.-x. Yang, N. Han, M. Fang, H. Lin, H.-Y. Cheung, S. Yip, E.-J. Wang, T. Hung, C.-Y. Wong and J. C. Ho, *Nat. Commun.*, 2014, **5**, 5249.
32 Z.-x. Yang, F. Wang, N. Han, H. Lin, H.-Y. Cheung, M. Fang, S. Yip, T. Hung, C.-Y. Wong and J. C. Ho, *ACS Appl. Mater. Interfaces*, 2013, **5**, 10946–10952.
33 Y. Meng, C. Lan, F. Li, S. Yip, R. Wei, X. Kang, X. Bu, R. Dong, H. Zhang and J. C. Ho, *ACS Nano*, 2019, **13**, 6060–6070.
34 W.-K. Hong, J. Yoon and T. Lee, *Nanotechnology*, 2015, **26**, 125202.
35 C. Han, D. Xiang, M. Zheng, J. Lin, J. Zhong, C. Haur Sow and W. Chen, *Nanotechnology*, 2015, **26**, 095202.
36 H. Qian, Y. Wang, Y. Fang, L. Gu, R. Lu and J. Sha, *J. Appl. Phys.*, 2015, **117**, 164308.
37 K. Kim, P. C. Debnath, S. Kim and S. Y. Lee, *Appl. Phys. Lett.*, 2011, **98**, 113109.
38 P.-C. Chang, Z. Fan, C.-J. Chien, D. Stichtenoth, C. Ronning and J. G. Lu, *Appl. Phys. Lett.*, 2006, **89**, 133113.
39 S. Song, W.-K. Hong, S.-S. Kwon and T. Lee, *Appl. Phys. Lett.*, 2008, **92**, 263109.
40 D. Kälblein, R. T. Weitz, H. J. Böttcher, F. Ante, U. Zschieschang, K. Kern and H. Klauk, *Nano Lett.*, 2011, **11**, 5309–5315.
41 S. Parthiban and J.-Y. Kwon, *J. Mater. Res.*, 2014, **29**, 1585–1596.
42 M. Zhou, H. Zhu, Y. Jiao, Y. Rao, S. Hark, Y. Liu, L. Peng and Q. Li, *J. Phys. Chem. C*, 2009, **113**, 8945–8947.
43 P. K. Mishra, S. Ayaz, B. Kissinquinker and S. Sen, *J. Appl. Phys.*, 2020, **127**, 154501.
44 N. Han, J. J. Hou, F. Wang, S. Yip, Y.-T. Yen, Z.-x. Yang, G. Dong, T. Hung, Y.-L. Chueh and J. C. Ho, *ACS Nano*, 2013, **7**, 9138–9146.
45 J. J. Hou, N. Han, F. Wang, F. Xiu, S. Yip, A. T. Hui, T. Hung and J. C. Ho, *ACS Nano*, 2012, **6**, 3624–3630.
46 Z. Fan, J. C. Ho, T. Takahashi, R. Yerushalmi, K. Takei, A. C. Ford, Y.-L. Chueh and A. Javey, *Adv. Mater.*, 2009, **21**, 3730–3743.
47 J. S. Lee, S. Chang, S. Koo and S. Y. Lee, *IEEE Electron Device Lett.*, 2010, **31**, 225–227.
48 K. Nomura, A. Takagi, T. Kamiya, H. Ohta, M. Hirano and H. Hosono, *Jpn. J. Appl. Phys.*, 2006, **45**, 4303–4308.
49 S. Deng, R. Chen, G. Li, Z. Xia, M. Zhang, W. Zhou, M. Wong and H. Kwok, *IEEE Trans. Electron Devices*, 2017, **64**, 3174–3182.
50 Z. Zheng, L. Gan, H. Li, Y. Ma, Y. Bando, D. Golberg and T. Zhai, *Adv. Funct. Mater.*, 2015, **25**, 5885–5894.
51 J. B. K. Law and J. T. L. Thong, *Appl. Phys. Lett.*, 2006, **88**, 133114.
52 X.-W. Fu, Z.-M. Liao, Y.-B. Zhou, H.-C. Wu, Y.-Q. Bie, J. Xu and D.-P. Yu, *Appl. Phys. Lett.*, 2012, **100**, 223114.
53 C. Park, J. Lee, H.-M. So and W. S. Chang, *J. Mater. Chem. C*, 2015, **3**, 2737–2743.
54 Y. Wang, Y. Chen, W. Zhao, L. Ding, L. Wen, H. Li, F. Jiang, J. Su, L. Li, N. Liu and Y. Gao, *Nano-Micro Lett.*, 2016, **9**, 11.
55 T. Cossuet, J. Resende, L. Rapenne, O. Chaix-Pluchery, C. Jiménez, G. Renou, A. J. Pearson, R. L. Z. Hoye, D. Blanc-Pelissier, N. D. Nguyen, E. Appert, D. Muñoz-Rojas, V. Consonni and J.-L. Deschanvres, *Adv. Funct. Mater.*, 2018, **28**, 1803142.
56 B. Zhao, F. Wang, H. Chen, L. Zheng, L. Su, D. Zhao and X. Fang, *Adv. Funct. Mater.*, 2017, **27**, 1700264.
57 X. Shen, L. Duan, J. Li, X. Zhang, X. Li and W. Lü, *Mater. Res. Express*, 2019, **6**, 045002.
58 S. Dhar, T. Majumder and S. P. Mondal, *ACS Appl. Mater. Interfaces*, 2016, **8**, 31822–31831.
59 A. Costas, C. Florica, N. Preda, N. Apostol, A. Kuncser, A. Nitescu and I. Enculescu, *Sci. Rep.*, 2019, **9**, 5553.
60 S. Park, S. Kim, G.-J. Sun, D. B. Byeon, S. K. Hyun, W. I. Lee and C. Lee, *J. Alloys Compd.*, 2016, **658**, 459–464.
61 T. Gao, Q. Zhang, J. Chen, X. Xiong and T. Zhai, *Adv. Opt. Mater.*, 2017, **5**, 1700206.
62 K. Liu, M. Sakurai, M. Liao and M. Aono, *J. Phys. Chem. C*, 2010, **114**, 19835–19839.
63 S. C. Rai, K. Wang, Y. Ding, J. K. Marmon, M. Bhatt, Y. Zhang, W. Zhou and Z. L. Wang, *ACS Nano*, 2015, **9**, 6419–6427.
64 T. D. Dao, C. T. T. Dang, G. Han, C. V. Hoang, W. Yi, V. Narayanamurti and T. Nagao, *Appl. Phys. Lett.*, 2013, **103**, 193119.
65 O. Lupan, V. Cretu, V. Postica, M. Ahmadi, B. R. Cuenya, L. Chow, I. Tiginyanu, B. Viana, T. Pauporté and R. Adelung, *Sens. Actuators, B*, 2016, **223**, 893–903.